Role of laser scan strategies in defect control, microstructural evolution and mechanical properties of steel matrix composites prepared by laser additive manufacturing

Hong-yu Chen, Dong-dong Gu, Qing Ge, Xin-yu Shi, Hong-mei Zhang, Rui Wang, Han Zhang, and Konrad Kosiba

View the article online at SpringerLink or IJMMM Webpage.

Articles you may be interested in

Hui-ping Duan, Xiao Liu, Xian-zhe Ran, Jia Li, and Dong Liu, Mechanical properties and microstructure of 3D-printed high Co-Ni secondary hardening steel fabricated by laser melting deposition, *Int. J. Miner. Metall. Mater.*, 24(2017), No. 9, pp. 1027-1033. https://doi.org/10.1007/s12613-017-1492-4

Dong-tao Wang, Hai-tao Zhang, Lei Li, Hai-lin Wu, Ke Qin, and Jian-zhong Cui, The evolution of microstructure and mechanical properties during high-speed direct-chill casting in different Al-Mg$_2$Si *in situ* composites, *Int. J. Miner. Metall. Mater.*, 25(2018), No. 9, pp. 1080-1089. https://doi.org/10.1007/s12613-018-1659-7

A. R. Sufizadeh and S. A. A. Akbari Mousavi, Microstructures and mechanical properties of dissimilar Nd:YAG laser weldments of AISI4340 and AISI316L steels, *Int. J. Miner. Metall. Mater.*, 24(2017), No. 5, pp. 538-549. https://doi.org/10.1007/s12613-017-1435-0

A. I. Noskov, A. Kh. Gilmutdinov, and R. M. Yanbaev, Effect of coaxial laser cladding parameters on bead formation, *Int. J. Miner. Metall. Mater.*, 24(2017), No. 5, pp. 550-556. https://doi.org/10.1007/s12613-017-1436-z

Ze-an Zhou, Wan-tang Fu, Zhe Zhu, Bin Li, Zhong-ping Shi, and Shu-hua Sun, Excellent mechanical properties and resistance to cavitation erosion for an ultra-low carbon CrMnN stainless steel through quenching and partitioning treatment, *Int. J. Miner. Metall. Mater.*, 25(2018), No. 5, pp. 547-553. https://doi.org/10.1007/s12613-018-1601-z

Xiao-feng Wang, Ming-xing Guo, Cun-qiang Ma, Jian-bin Chen, Ji-shan Zhang, and Lin-zhong Zhuang, Effect of particle size distribution on the microstructure, texture, and mechanical properties of Al–Mg–Si–Cu alloy, *Int. J. Miner. Metall. Mater.*, 25(2018), No. 8, pp. 957-966. https://doi.org/10.1007/s12613-018-1645-0

IJMMM WeChat   QQ author group

Role of laser scan strategies in defect control, microstructural evolution and mechanical properties of steel matrix composites prepared by laser additive manufacturing

Hong-yu Chen[1,2], *Dong-dong Gu*[1,2], *Qing Ge*[1,2], *Xin-yu Shi*[1,2], *Hong-mei Zhang*[1,2], *Rui Wang*[1,2], *Han Zhang*[1,2], *and Konrad Kosiba*[3]

1) College of Materials Science and Technology, Nanjing University of Aeronautics and Astronautics, Nanjing 210016, China
2) Jiangsu Provincial Engineering Laboratory for Laser Additive Manufacturing of High-Performance Metallic Components, Nanjing University of Aeronautics and Astronautics, Nanjing 210016, China
3) Leibniz IFW Dresden, Institute for Complex Materials, Helmholtzstr. 20, 01069 Dresden, Germany

Abstract: Steel matrix composites (SMCs) reinforced with WC particles were fabricated via selective laser melting (SLM) by employing various laser scan strategies. A detailed relationship between the SLM strategies, defect formation, microstructural evolution, and mechanical properties of SMCs was established. The laser scan strategies can be manipulated to deliberately alter the thermal history of SMC during SLM processing. Particularly, the involved thermal cycling, which encompassed multiple layers, strongly affected the processing quality of SMCs. S-shaped scan sequence combined with interlayer offset and orthogonal stagger mode can effectively eliminate the metallurgical defects and retained austenite within the produced SMCs. However, due to large thermal stress, microcracks that were perpendicular to the building direction formed within the SMCs. By employing the checkerboard filling (CBF) hatching mode, the thermal stress arising during SLM can be significantly reduced, thus preventing the evolution of interlayer microcracks. The compressive properties of fabricated SMCs can be tailored at a high compressive strength (~3031.5 MPa) and fracture strain (~24.8%) by adopting the CBF hatching mode combined with the optimized scan sequence and stagger mode. This study demonstrates great feasibility in tuning the mechanical properties of SLM-fabricated SMCs without varying the set energy input, e.g., laser power and scanning speed.

Keywords: laser additive manufacturing; selective laser melting; scan strategy; defect control; mechanical property

1. Introduction

The 1.2767L alloy is a medium-carbon, cold-work steel applied to manufacture tools for forging, coining, cutting, and plastic molding. These tools are subjected to extremely high loads which arise rapidly and involve high thermal gradients [1]. The fabricated tools must repeatedly withstand such loading conditions without large deformation and early failure. One strategy to fulfill such requirements is to introduce hard ceramic particles into the steel matrix to achieve the preparation of high-performance steel matrix composites (SMCs).

SMCs are commonly fabricated by casting or powder metallurgical techniques [2]. These techniques usually enable the preparation of SMC components with coarse microstructures and heterogeneously distributed ceramic particles [3].

Selective laser melting (SLM) is a fast-emerging additive manufacturing (AM) technology allowing the rapid fabrication of three-dimensional (3D) SMC parts with unlimited geometrical freedom directly from composite powder [4]. Defined volumes of each layer are successively melted by the scanning laser beam in accordance with the slice information of the respective CAD file [5]. Thus, SLM shows a high potential for the near net-shape fabrication of high-performance SMC parts with complex geometries, which cannot be readily prepared by the other traditional manufacturing techniques [6]. The development and production period of the component and cost can be also reduced by utilizing SLM. Therefore, SLM techniques, which allow the fabrication of geometrically and highly complex SMC components, have been and are gaining significant attention in the industry and academia [7].

Ⓐ Springer

Numerous efforts have been made to improve the processing quality and mechanical properties of ceramic particle-reinforced SMC parts to promote their practical application across various industrial fields [8–10]. Particularly, WC is considered as a suitable reinforcement for steel materials owing to its high melting point, thermal stability, strength, hardness, and good wettability. Yan *et al.* [11] investigated the tribological properties of SLM-fabricated WC/Fe composites, and their results revealed that the good adhesion of WC particles through their reaction layer to the Fe-based matrix results in a better wear resistance compared with single iron-based alloy. Wang *et al.* [12] revealed that the main challenge in developing high-performance WC-reinforced SMCs is controlling the evolution of cracks formed in the reaction layers between the WC particles and iron-based matrix. Rapid melting and subsequent solidification are inherent to SLM processing and induce significant thermal gradients. These thermal gradients can result in the evolution of large residual stress fields within the SLM part, and they are especially pronounced in WC-reinforced SMC parts, where a difference exists in the thermal conductivity between steel matrix and WC particles. The formation of pronounced residual stresses results in the evolution of cracks, which generally propagate along the interface between WC and iron-based matrix [10]. In this situation, the WC particles cannot act in a load-bearing manner, and their contribution to the mechanical properties of the composite material is highly limited. Additionally, residual stresses can lead to deformation, especially severe warping, and failure of parts during the AM processing and/or subsequent post-processing. Many investigations focused on optimizing the processing parameters, such as the laser energy density [8], starting size [9], and additive amount of reinforcements [10], to solve these problems. In addition to these main parameters, the laser scan strategy is considered to be another key factor for the fabrication of high-performance SLM parts. Kruth *et al.* [13] reported the origin of residual stress within SLM-fabricated parts and the effect of exposure strategy, sector scanning order, and post-scanning on the processing quality of iron-based parts. They observed that an appropriate scan strategy induces a significant alleviation in thermal deformations, and the vaporization effect of metal is utilized to restrain the balling effect. Zhang *et al.* [14] developed a consecutive sub-sector scan mode with adjustable scan lengths for SLM. They revealed that this scan pattern increases the temperature in small subsectors, facilitating the complete melting of the powder material. Qian *et al.* [15] studied the so-called helix scan strategy applied to SLM and revealed that it alleviates the deformation of the melted layers. Su and Yang [16] developed an interlayer offset stagger (IOS) mode for the laser scan and demonstrated that this stagger mode can improve the metallurgical bonding between adjacent melting tracks; as a result, the overmelting phenomenon and intertrack de-

fects can be eliminated. Prashanth *et al.* [17] analyzed the crack propagation mechanism of Al–12Si tensile specimens fabricated at different laser scan strategies. They revealed the influence of contour on the tensile properties of SLM-fabricated parts. However, the abovementioned studies did not provide a unified conclusion clarifying the strategy–processability–property correlation with different measurement strategies, materials, and parameters being used throughout. Several publications [18–20] offered contradicting results with regard to the relation between the direction of greatest stress, i.e., the direction of stress accumulation, and applied scan vectors. Thereby, the interaction between laser scan routes, defect formation, microstructure, and the resulting mechanical properties of SLM-fabricated SMC parts still needs to be extensively investigated. Measures permitting the optimization of the mechanical properties of SMC components *in-situ* during SLM fabrication without changing the set energy input (i.e., without changing the main laser parameters, including laser power and scan speed) must be identified.

In this study, WC particles were used to reinforce 1.2767L steel, and the powder mixture was processed via SLM. A method was developed to tune the microstructure and mechanical properties of WC-reinforced SMCs by optimizing the laser scan strategies at which the following parameters were varied: (1) scan sequence, (2) stagger mode, and (3) hatching mode. The specimens with different laser scan strategies were examined with respect to the formation of defects and residual stress within the SMC parts. Furthermore, the microstructural evolution and compressive properties of the fabricated SMCs were assessed. The variations in thermal history during the melting of the powder layer and the subsequent solidification using different laser scan strategies were investigated to provide a deeper understanding of the formation of microstructural defects and stress accumulation behavior within selectively melted specimens. The possible fracture mechanism of SMC parts fabricated by different scan strategies was also discussed. This work sets the basis for the development of optimized scan strategies to achieve the reliable manufacturing of high-performance SMC components via SLM.

2. Experimental

2.1. Powder materials

Spherical gas-atomized 1.2767L tool steel powder (TLS Technik GmbH, Germany) with a mean particle size D50 of 21.6 μm and spherical WC powder (Zhuzhou Cemented Carbides Group Co., Ltd., China) with an average size of around 600 nm were used in this study. Pulverisette 6 planetary mono-mill (Fritsch GmbH, Germany) was applied in this study to prepare the WC/steel composite powder containing 2wt% WC. The detailed procedures and parameters used in
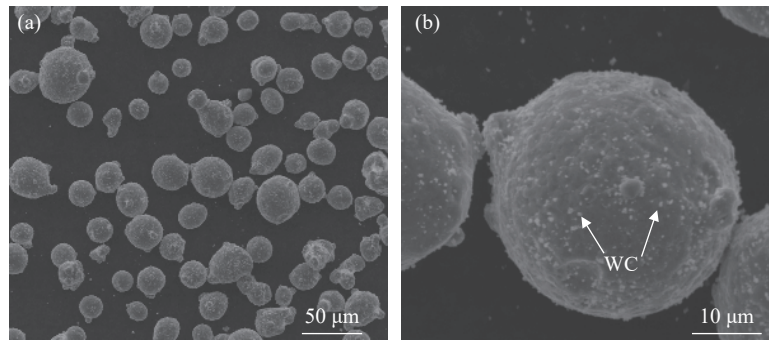
Fig. 1.   (a) Representative morphology of the composite powder prepared via ball milling; (b) micro-sized WC particles uniformly dispersing on the surface of the steel powder.

ball milling were given in our previous study [3]. Fig. 1 shows the as-prepared composite powder. The micro-sized WC particles uniformly dispersed on the surface of the steel powder.

2.2. SLM process

The SLM process was performed using a self-developed SLM-150 device consisting of a YLR-500 ytterbium fiber laser with a power of ~500 W and a spot size of 70 μm (IPG Laser GmbH, Germany). The detailed processing procedures were given in our previous work [3]. Different laser scan strategies were implemented via altering the laser scan sequence, stagger mode, and hatching mode during SLM. By employing laser scan sequences, we can determine whether the adjacent laser scan lines of the same layer are continuous. The scan sequences used were the so-called Z-shaped scan (ZS, all scan tracks oriented parallel to each other and discontinuous) and S-shaped scan (SS, parallel and continuous scans), as shown in Figs. 2(a) and 2(b), respectively. The stagger mode determines how the laser scan routes in adjacent layers stagger with each other. The IOS (scan lines in adjacent layers staggered by a certain distance at half of the hatch distance) and orthogonal stagger (OS, 90° rotation scan direction between adjacent layers) were conducted in this study, as shown in Figs. 2(c) and 2(d), respectively. The hatching mode determines how the laser line fills the pattern of the cross-sections of the part based on the CAD data. No pattern filling (NPF, no special fill pattern is used), contour filling (CF, all the scan tracks are parallel to the sliced contours, and the distance between adjacent scan lines is equal to the hatch distance), and checkerboard filling (CBF, the same layer is divided into numerous small checkerboards, and these checkerboards are laser melted in accordance with a predetermined sequence) were performed in this work (Figs. 2(e), 2(f), and 2(g), respectively). All the laser scan strategies were applied with the same processing parameters of laser power (P) at 450 W, scan speed (v) at 1800 mm/s, hatch distance (s) at 50 μm, and layer thickness (h) at 40 μm. The 9
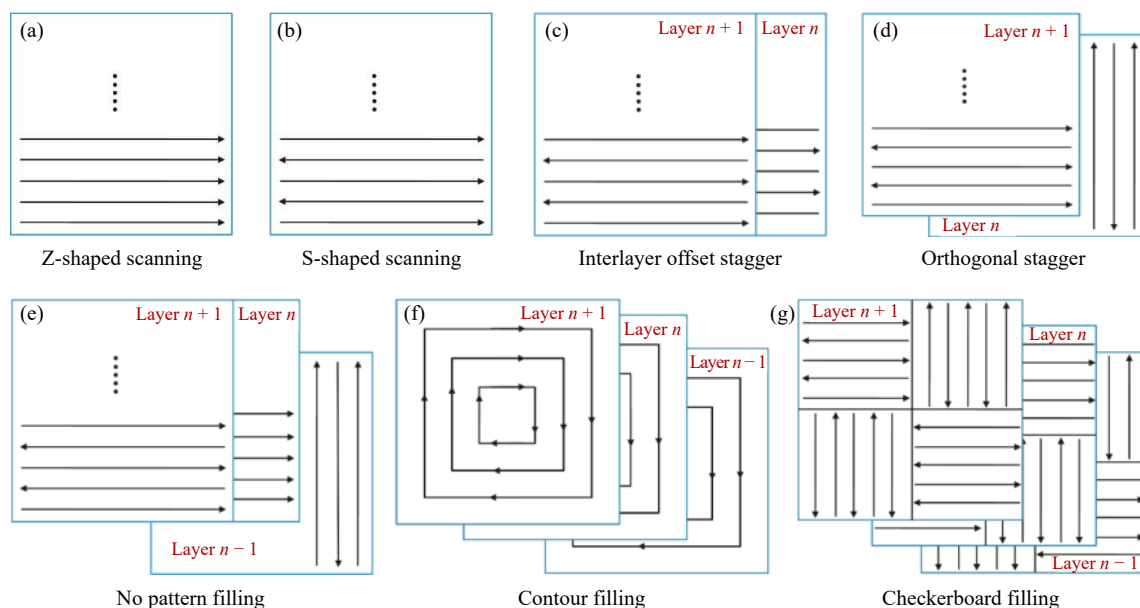

Fig. 2.   Different laser scan strategies implemented via altering the laser scan sequence, stagger mode, and hatching mode during SLM: (a) ZS; (b) SS; (c) IOS; (d) OS; (e) NPF; (f) CF; (g) CBF.

mm × 9 mm × 4 mm specimens were built to characterize the defect formation and microstructure of SLM-processed SMCs. Additionally, cylindrical samples (ϕ3 mm, length of 6 mm) were fabricated along the building direction to characterize the mechanical properties of the SMCs.

2.3. Structural characterization

The distribution of defects within SLM-processed SMCs was tested by computed X-ray tomography (μ-CT; phoenix nanotom m, GE, USA) and the corresponding densification levels was also determined. X-ray diffraction (XRD; Co K$_{\alpha 1}$ radiation; STOE Stadi P, Germany) was performed on the upper surface of SMC specimens to identify the phases constitution. Field emission scanning electron microscopy (FE-SEM; Hitachi, Japan) was used to characterize the microstructures of SMC samples. The SEM images were processed by ImageJ software, and then the distribution of sec-

ondary phases can be identified. The upper surfaces of SMC samples were also observed by FE-SEM.

2.4. Residual stress measurement

As the temperature (*T*) fell rapidly during SLM, the top region shrunk further, but this shrinkage was restrained by its bottom region. Thus, tensile and compressive residual stresses occurred at the top and bottom regions, respectively (Fig. 3(a)) [21]. The tensile residual stress, in most cases, deteriorates the mechanical property of SLM-processed parts. A D8-ADVANCE X-ray diffractometer (Bruker AXS GmbH, Germany) was used to identify the highest residual stresses on the top surface of SMC samples. The residual stresses (σ) were measured at different places to show the stress distribution (Fig. 3(b)). The residual stress at each point along the X (σ_X) or Y (σ_Y) directions was measured thrice, and the average of the three readings was recorded.
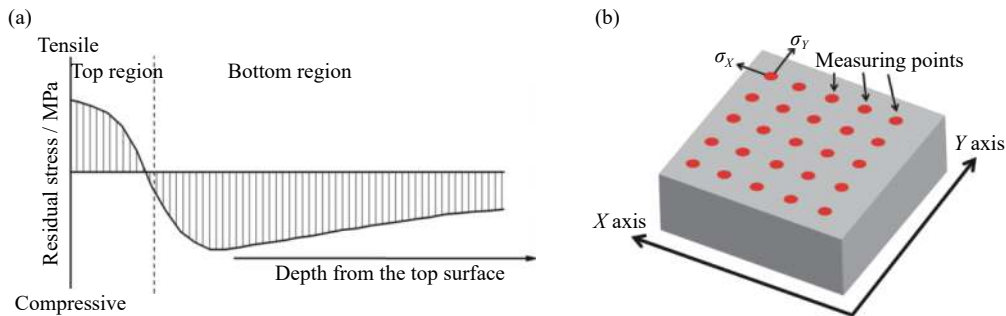

Fig. 3. (a) Theoretical residual stress distribution along the building direction; (b) schematic of the experiments for residual stress distribution testing along the *X* and *Y* directions.

2.5. Mechanical testing

The MTS Landmark 370 (MTS Systems Corporation, USA) was used to perform quasi-static compression tests on the SMC samples at room temperature. The upper and bottom surfaces of all compression samples were lubricated with zinc stearate prior to compression testing to alleviate the frictional effect. The displacement rate was 0.1 mm/min. At least three specimens were tested to ensure the reproducibility of the data. The fracture surfaces were observed by FE-SEM.

3. Numerical simulation

The quasi-stationary temperature field and temperature gradient when using ZS and SS modes were calculated using the computational fluid dynamics software FLUENT 6.3.26 to investigate the effect of laser scan sequence on the thermal

history of melting and solidification process of the powder layer. The mathematical model, governing equations, convection and radiation, evaporation modes, Gaussian heat source, and the convergence principle of numerical calculations have been proposed in our previous study [22] in detail. Table 1 lists the thermophysical properties of as-used materials. The thermal conductivity of WC is 121 W·m^{-1}·K^{-1} with temperature below the melting point, while the thermal conductivities of steel matrix under different temperatures used in the numerical simulation were referred to the data in Ref. [27].

4. Results and discussion

4.1. Effect of laser scan strategy on defect formation within SLM-fabricated SMCs

The laser scan sequence determined the sequence of melt

Table 1.   As-used material properties

Material	Laser absorptivity	Density / (g·cm^{-3})	Melting point / K	Melting heat / (J·g^{-1})	Ambient temperature, T_0 / K	Marangoni coefficient, $\partial\gamma/\partial T$ / (N·m^{-1}·K^{-1})
WC	0.61 [23]	15.6	3134	590 [25]	300	—
Steel	0.47 [24]	7.9	1808	269		-0.52×10^{-3} [26]

tracks. Powder particles absorbed laser energy until they were melted. Hence, the laser scan sequence determined the heat transfer within the powder bed, thereby greatly affecting the final processing quality of the SLM-fabricated SMCs. Fig. 4 highlights the surface morphologies of the SMC samples fabricated using ZS scan sequence (named SMC-ZS) and SS scan sequence (named SMC-SS). Surfaces at the center and marginal region of the top surface were depicted. A severe "marginal balling effect" was observed at the margin of the SMC-ZS sample, whereas the SMC-SS sample showed a smooth and stable margin. The SMC-ZS sample showed a rougher top surface compared with the SMC-SS sample. The distinction in the surface morphology between SMC-ZS and -SS samples indicated that the laser scan sequence played a vital role in SLM processing of the composite powder. The scanning path of laser beam influenced the thermomechanical behaviors of the laser-processed powder region and thus affected the final processing quality of the manufactured SMCs. Fig. 5 illustrates the thermal behavior of the molten pool, namely, the temperature distribution and gradient along the Y-direction dependent on the laser scan sequence. The molten pool for the SMC-ZS sample showed a

similar maximum temperature to the SMC-SS sample during SLM, whereas the thermal gradients along the Y-direction largely differed. A larger thermal gradient ($(\partial T/\partial y)_{\max} = -3.28 \times 10^7$ K/m) along the Y-direction of the molten pool evolved within the SMC-ZS sample in comparison with the SMC-SS sample ($(\partial T/\partial y)_{\max} = -2.01 \times 10^7$ K/m). Large thermal gradient always leads to an evolution of a pronounced gradient in surface tension of the liquid. Thus, the melt turns into metallic agglomerates with spherical shape to minimize the surface energy, hence resulting in the evolution of the so-called "marginal balling effect" (MBE) [28]. The MBE obstructed the movement of the powder-spreading device when a fresh powder layer was deposited, thus facilitating the formation of metallurgical defects within the SMC sample. When SMCs were fabricated using the SS sequence, this undesirable effect can be effectively alleviated, because a reduced temperature gradient is effective within the molten pool. Adjacent melting tracks were then preheated, resulting in the decreased surface tension gradient and capillary instability of the melt during the synthesis of SMC-SS sample, leading to an enhanced surface quality of the final SMC components.
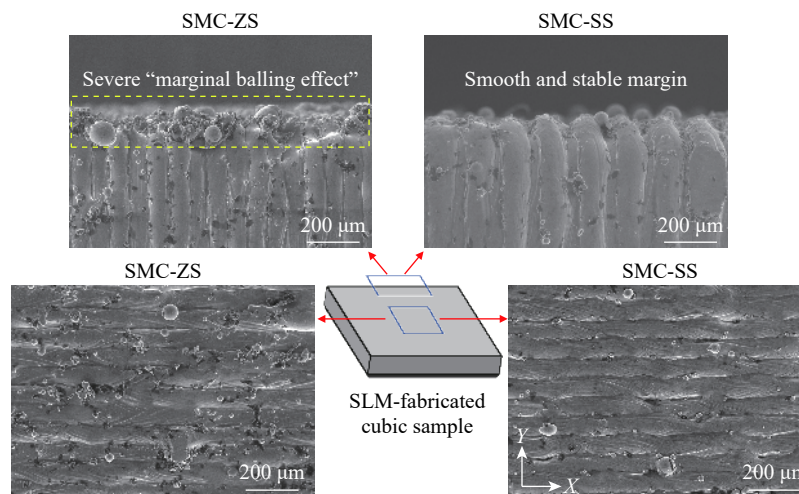

Fig. 4.   FE-SEM images showing the surface morphologies of SLM-fabricated SMCs using ZS and SS laser scanning sequences.

Residual stresses and deformations are inherent to SLM-manufactured components and limit their application. Highly localized laser energy input generally causes large thermal gradients to evolve in the manufactured material, ultimately leading to the generation of residual stresses during SLM processing. With the repeated layer-by-layer AM processing, these stresses can accumulate and may lead to serious distortion and failure, such as layer cracking or delamination [29]. Therefore, the stagger mode of the laser scan between adjacent layers should be well designed to optimize the local heat distribution during SLM. IOS is an effective stagger mode to improve the surface quality and reduce metallurgical defects in SLM-fabricated SMC parts while achieving a homogen-

eous Gaussian distribution of laser energy at the adjacent processing layers [16]. IOS avoids the repetition of melting tracks at the same position along the building direction and eliminates defects that can form at overlapping regions. Without the IOS mode, the laser energy density at the center of the melting track was notably larger than that at the overlapping regions. Therefore, metallurgical defects tended to form at the overlapping region without sufficient laser energy input (Fig. 6(a)). By contrast, IOS enabled a uniform energy distribution at the processed layer. Overlapping regions within the last processed layer were melted when the stagger laser scan mode, which entails the elimination of interlayer pores, was applied and hence improved the processing qual-
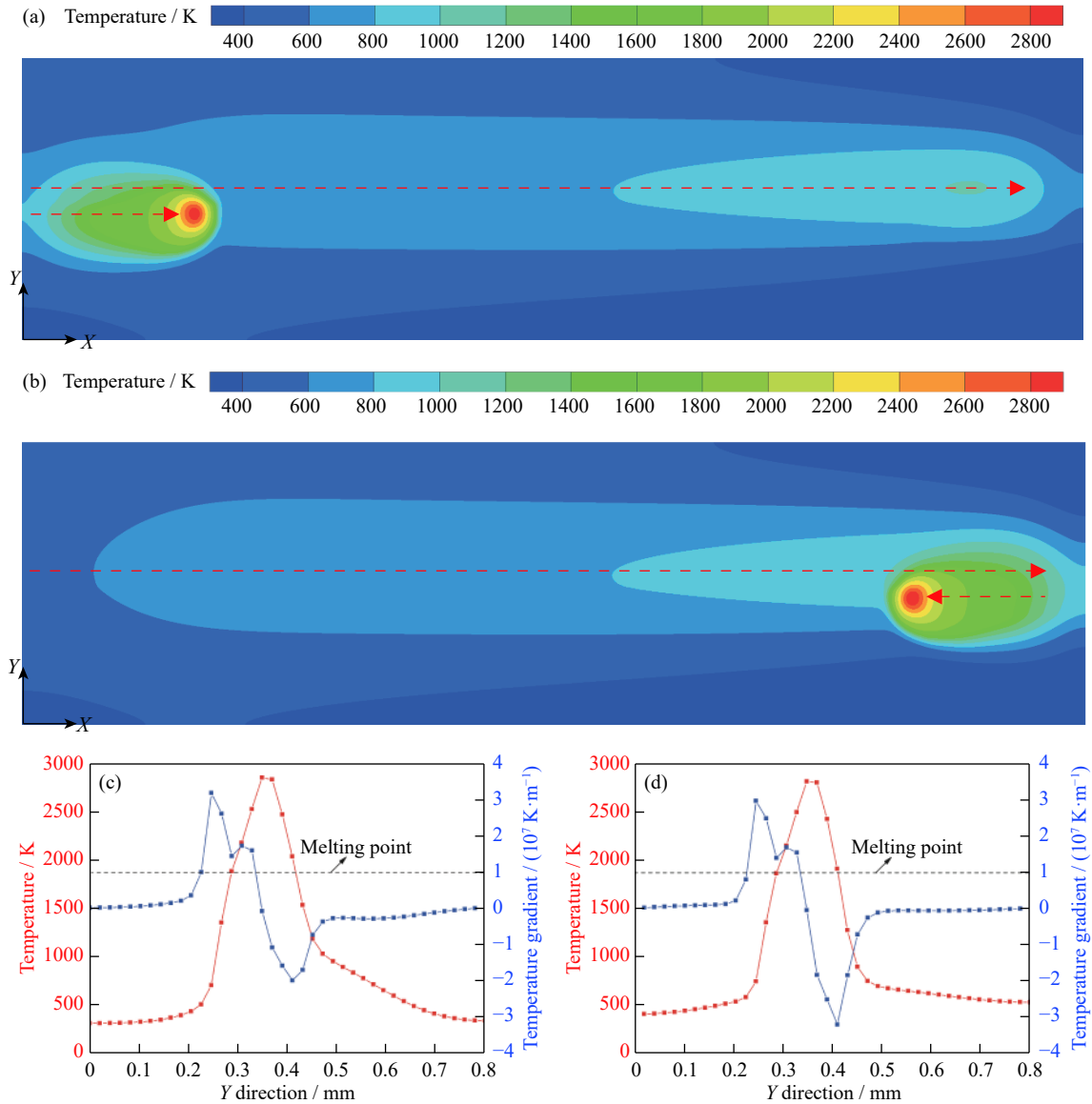
Fig. 5. **Temperature contour plots in top view, temperature distributions, and temperature gradients along the *Y* direction: (a, c) ZS sequence; (b, d) SS sequence.**

ity of the SLM-fabricated SMC sample (SMC-IOS, Fig. 6(b)).

In addition to IOS, OS is a useful laser stagger mode that can balance the residual stress within SLM-fabricated parts [30]. Controlling the residual stresses avoids the warping of the current layer from the previous one. As a consequence,
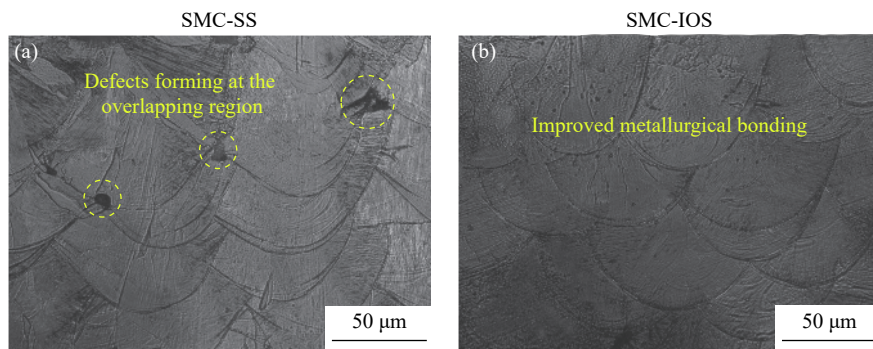

Fig. 6. **Different metallurgical bonding behaviors of the SMC samples processed (a) without and (b) with IOS mode.**

the interlayer cracking within the SMC samples can be circumvented. According to the literature [31], a relationship exists between the length of the scan line and the evolving stress within the SMC samples:

$$\vec{P} = \frac{KDH}{C} \int_0^{t_c} \vec{v_t}\,\mathrm{d}t \tag{1}$$

where $\vec{P}$ is the residual stress of a scan path along the single direction, t_c is the consumption time when the laser beam moves from the start scan position to the current position, $\vec{v_t}$ is the vector velocity at time t along the scan direction, H is the average melting thickness of the scan path, D is the average melting width of the scan path, C is the thermal conductivity of the metal powder, and K is a material specific constant. Eq. (1) indicates that the laser scanning along a single direction resulted in the accumulation of residual stress. Fig. 7 illustrates the comparison of the residual stress in SMC samples, which were fabricated with and without OS stagger mode, at their top surface along the X and Y directions. The highest σ_X and σ_Y of SMC sample with OS mode were both detected at around 300 MPa. By contrast, the sample without OS displayed a nonuniform stress distribution. The highest σ_X (390 MPa) was considerably larger than the highest σ_Y (234 MPa), indicating that the accumulation of residual stress generally occurred in directions parallel to the scan direction. OS entailed a more balanced distribution of the residual stress within the SLM-fabricated parts compared with IOS. Therefore, the directional distortion and potential failure of SMC samples can be reduced.
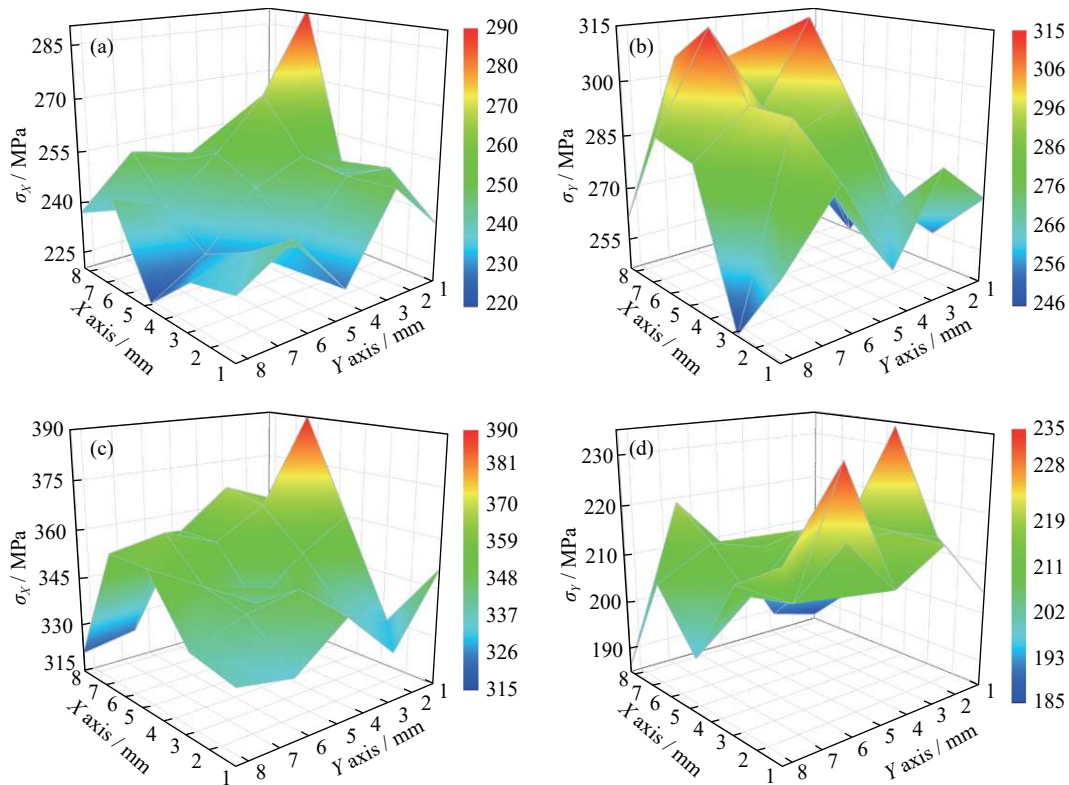

Fig. 7.   Residual stresses at different measuring points along the X and Y directions of the SMC samples fabricated (a, b) with and (c, d) without OS mode.

After selecting the best laser scan sequence and stagger mode for fabricating SMCs by SLM, the optimized filling pattern to hatch the cross-section of the 3D mode of SMCs parts should be determined. NPF, CF, and CBF are the most used hatching modes in SLM [29]. Thus, in the following, the defect formation and stress development within SMCs samples prepared by NPF, CF, and CBF hatching mode (further named SMC-NPF, SMC-CF, and SMC-CBF) were investigated. All these hatching modes were applied with SS, IOS, and OS scanning strategies to reduce the formation of metallurgical defects and to balance the thermal stress within the SMC parts during SLM.

The surface morphologies of SLM-processed SMCs were characterized using SEM to further investigate the dependence of defect formation on the hatching mode. The size-distribution of the pores inherent to the SMC specimen was identified by μ-CT. Fig. 8 reveals the corresponding results for SMC samples fabricated by different hatching modes. Table 2 lists the statistical residual stresses along the X- and Y-axis obtained on the surface of SMC samples prepared by different hatching modes. The surface of SMC-CF specimen showed high roughness and apparent pores, which mainly

formed around the center region, with a size of about 80 μm in diameter (Fig. 8(a)). From the μ-CT reconstruction map, the pores were distributed throughout the SMC-CF specimen (Fig. 8(b)), which had a relatively low density (~92.8%). When a rectangle-shaped layer was hatched in accordance with the CF, residual stresses evolved along the vertical direction of the scan path pointing toward the center of the rectangle contour [32]. This specific stress distribution led to the evolution of considerable bending stress (the average σ_X, $\overline{\sigma_X}$ = 263 MPa; the average σ_Y, $\overline{\sigma_Y}$ = 271 MPa) on the top surface of the SLM parts. The bending stress deteriorated the geometric accuracy and surface quality of SLM-fabricated SMCs, resulting in an unfavored metallurgical bonding between layers. As the scan line became increasingly shorter, which indicates its proximity toward the center region, the overheating phenomenon can easily occur because of the pronounced thermal accumulation effect, resulting in the formation of pore defects. By contrast, the SMC-NPF sample, which presented a smooth top surface (Fig. 8(c)), showed the highest relative density (~99.3%). In lieu of pores, microcracks with a length of about 1 mm can be observed (Fig. 8(d)). Vertically and horizontally oriented cracks with respect to the building direction were visible. According to the literature [33], large residual stresses within SMC ($\overline{\sigma_X}$ = 265 MPa; $\overline{\sigma_Y}$ = 287 MPa) easily caused an interruption of liquid film at the molten pool boundaries during solidification, which resulted in the formation of microcracks. The

SMC specimen, which was fabricated by employing the CBF hatching mode, showed a high densification level of 98.1% and a low residual stress ($\overline{\sigma_X}$ = 187 MPa; $\overline{\sigma_Y}$ = 176 MPa). The μ-CT reconstruction map demonstrated the fabrication of high-density SMC, in which several apparent pores were present, and no cracks can be observed (Fig. 8(f)). By employing the CBF mode, the SMC sample with a reduced residual stress can be fabricated, given that a decreased scan vector length is utilized. As inferred from Eq. (1), the value of $\int_0^{t_c} \vec{v_t}\,\mathrm{d}t$ decreases as the scan line becomes shorter. Thus, $|\vec{P}|$ was reduced along the corresponding scan direction. The reduced thermal stress prevented the SMC sample from early cracking and premature fracture during SLM processing. Nevertheless, controlling the overlapping between adjacent checkerboards is notably challenging. As depicted by the surface morphology of the appendant SMC specimen (Fig. 8(e)), key-hole-type defects were visible at these overlapping regions. Their formation is the major obstacle for the fabrication of fully dense SMC samples.

Table 2.   Overview of statistical residual stresses along the *X*- and *Y*-axis obtained at the surface of SMC samples prepared under different hatching modes

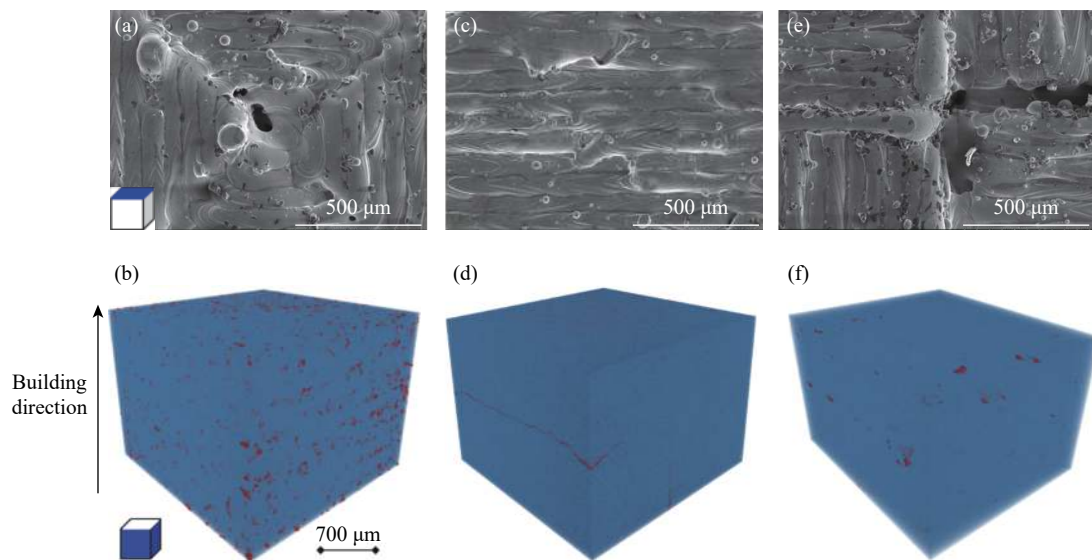| Hatching mode	σ_X / MPa	σ_Y / MPa
CF	263 ± 36	271 ± 39
NPF	265 ± 41	287 ± 35
CBF	187 ± 32	176 ± 34

Fig. 8.   Characteristic morphologies at the upper surface of SMC samples and the distributions of pores within SMC samples prepared under various hatching modes: (a, b) CF; (c, d) NPF; (e, f) CBF.

4.2. Effect of laser scan strategies on the microstructural evolution of SLM-fabricated SMCs

The laser scanning strategies determine the thermal history of the processed thin powder layer during melting and subsequent solidification, thus leading to different micro-

structural features of the SMC samples. Fig. 9 displays the typical XRD patterns of the SMC-CF, SMC-NPF, and SMC-CBF samples. The XRD data demonstrated that the microstructures of all fabricated SMC samples were composed of martensite as the main phase and retained austenite with a

low volume fraction. The content of retained austenite within SMCs varied depending on the hatching mode used. The SMC-CF sample contained about 27.8vol% retained austenite, which was almost twice those of the SMC-NPF (12.1vol%) and SMC-CBF (14.6vol%) samples. Martensite formed directly from the undercooled austenite, because extremely high cooling rates were effective during the rapid solidification of the molten pool [34]. During SLM processing of the overlying powder layer, heat was extracted through the previous solidified layer. Thereby, a fraction of the martensite was retransformed into austenite, which was retained within the solidified microstructure. From the variation of the content of retained austenite in different SMC samples, various laser scanning strategies caused varied thermal cycling behaviors during SLM, resulting in the differences in the phase constitution of the SMC samples. The residual heat effect, which resulted from the short scanning path at the center region of the SMC-CF sample, caused the heat flux to increase significantly. The heat flux originated from the molten regions and was extracted toward the building platform. Thus, the temperature of the center regions within the previously solidified layers reached values above the martensite start temperature (M_s). This condition resulted in the retransformation of martensite into austenite. By contrast, less thermal heat accumulated during the layer-by-layer fabrication within the SMC-NPF and SMC-CBF samples. Most martensite was not retransformed into austenite. Thus, the microstructures of SMC-NPF and SMC-CBF samples contained less retained austenite.
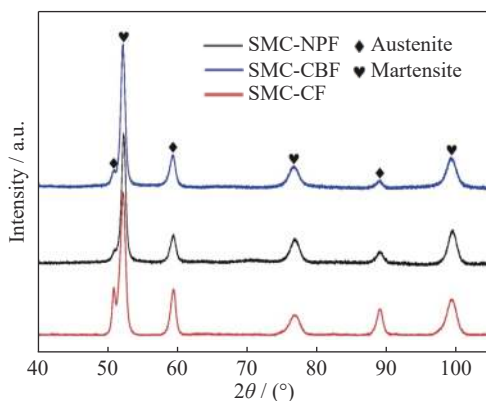

Fig. 9.   XRD spectra of SLM-fabricated SMC samples (center region) prepared under different laser hatching modes.

Fig. 10 shows the SEM images and corresponding ImageJ-processed images of the center region of the SLM-fabricated SMC samples prepared with different hatching modes after etching. The microstructures showed a cellular morphology with secondary phases precipitating along the cell boundaries. The martensite was etched out; thus, the typical martensitic lath structures were hardly visible. Our previous study [35] demonstrated that the secondary phases, which precipit-

ate along the cell boundaries, are $(Fe,W)_6C$-type carbides. During the rapid solidification process, W and C were segregated to the cell boundaries. There, they reacted with Fe, leading to the formation of $(Fe,W)_6C$-type carbidic network. However, the $(Fe,W)_6C$ carbides cannot be identified by XRD analysis because their low volume fraction in the SMCs was below the resolution limit of the XRD device used. Figs. 10(b), 10(d), and 10(f) show the distributions of $(Fe,W)_6C$ carbides within the iron-based matrix using ImageJ software. The laser scanning strategies significantly affected the final morphology of the Fe_2W_4C carbidic network. When the CF hatching mode was utilized, a significant amount of heat accumulated in the center region. Consequently, the carbides dissolved into the iron-based matrix, and the carbidic network became discontinuous. Additionally, compared with the SMC-NPF and SMC-CBF samples, the average size of the cell structure in SMC-CF sample was larger. This finding indicated that the pronounced residual heat effect resulted in the growth of the cell structure. By contrast, the carbidic network in SMC-NPF and SMC-CBF samples showed a decent continuity. The average sizes of the cell structures in SMC-NPF and SMC-CBF samples were 1.45 and 1.76 μm, respectively. The difference in the sizes of the cell structure indicated the different crystallization behaviors of the iron-based matrix. As described by Cheng *et al.* [29], the substrate experienced the highest minimum temperature when the CBF hatching mode was employed. In comparison with the other hatching modes, more time was needed to complete a layer using CBF, and thus, more heat was introduced into the substrate. The energy input was more concentrated when the laser sequentially filled the small checker areas, leading to a more pronounced residual heat effect between adjacent scanning tracks in the SMC-CBF sample in comparison with the SMC-NPF sample. Accordingly, the cell structures in SMC-CBF sample were promoted to grow or merge with each other, resulting in a coarser microstructure compared with the SMC-NPF sample.

4.3. Effect of laser scan strategies on mechanical properties of SLM-fabricated SMCs

Fig. 11 shows the representative engineering stress–strain curves of various SMC samples subjected to uniaxial compression. The fracture surfaces of compressive specimens were observed by SEM to reveal their corresponding fracture mechanism (Fig. 12). The compressive properties of SLM-fabricated SMCs depended on the laser scan strategy used. The SMC-CF sample showed the lowest compressive strength of ~2365.4 MPa and a limited fracture strain of ~21.2%. The low densification and high content of retained austenite were the main reasons for the poor compressive properties. The corresponding fracture surface presented evidently large voids with a size of ~80 μm (Fig. 12(a)). The void defects within the SMC-CF sample generally acted as
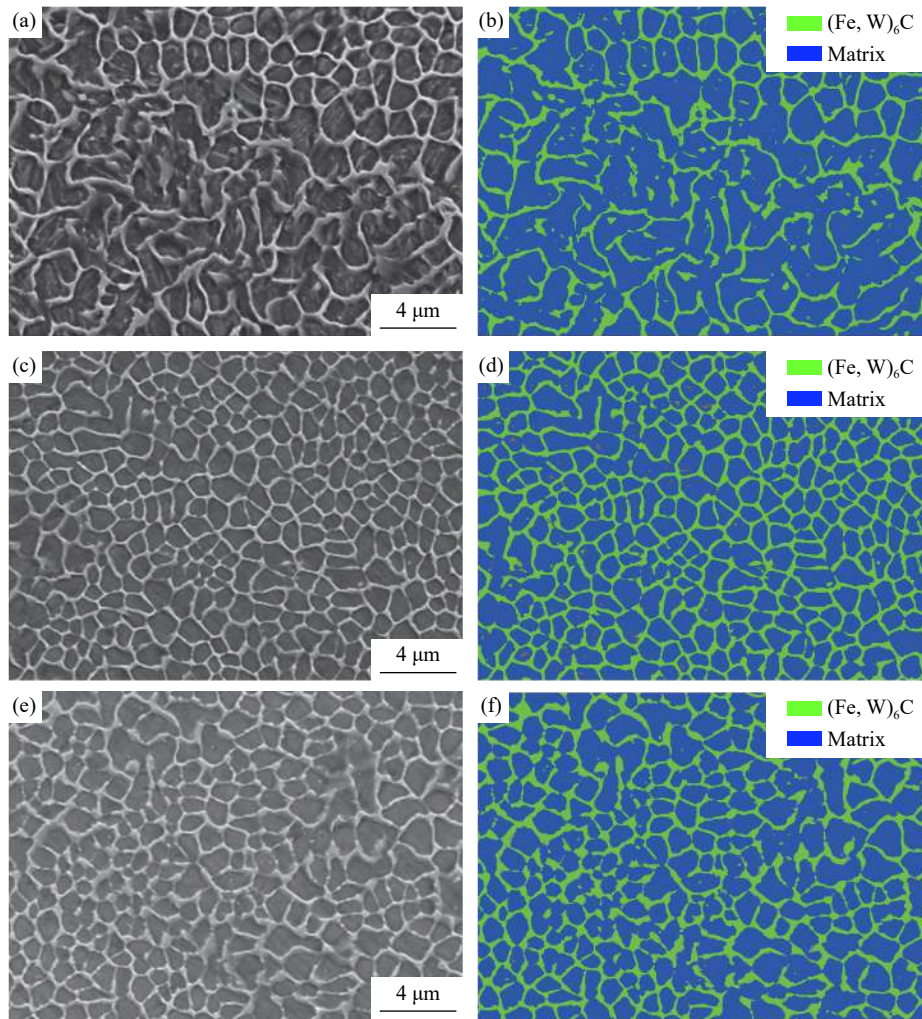
Fig. 10.   (a, c, e) SEM images and (b, d, f) corresponding ImageJ-processed images of the microstructures of the center region of SMC samples prepared at different laser hatching mode after etching: (a, b) CF; (c, d) NPF; (e, f) CBF.
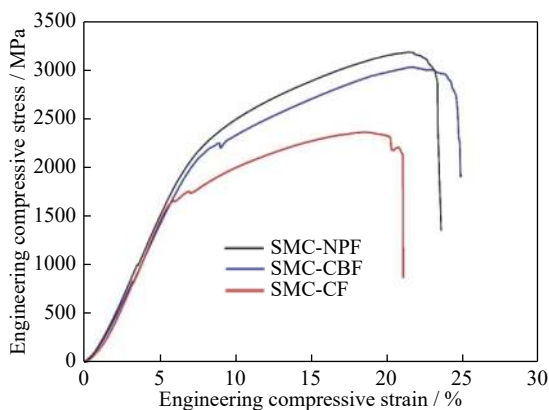

Fig. 11.   Typical compressive stress–strain curves of the SMC samples prepared using different laser scanning strategies.

stress concentrators during loading and as main sites for the initiation and rapid propagation of cracks. The retransformation of martensite into austenite, which was due to the residual heat effect during SLM, limited the martensitic hardening effect and resulted in a low strength of SMCs. Additionally, the large residual stress and attendant limited metallurgical bonding between adjacent layers also led to the early failure of SMCs. By contrast, the SMC-NPF and SMC-CF samples showed high compressive strength (~3184.3 and ~3031.5 MPa, respectively) and an improved fracture strain (~23.5% and ~24.8%, respectively). The high densification levels and low contents of retained austenite significantly strengthened the SMCs. Furthermore, their microstructures consisted of substantially refined grains (Figs. 10(c)–10(f)), involving high volume fractions of grain boundaries. As a result, the SMC-NPF and SMC-CBF samples showed increased strength. The work of Wang *et al.* [36] suggested that the cells in the SMC samples should be subgrains. Similar to grain boundaries, cell boundaries also contribute to the strengthening of the fabricated materials, with the segregation products at the cell boundaries (such as the M_6C carbide in this study) effectively hindering the movement of dislocations [37]. The ductility of the SMC-NPF sample was inferi-
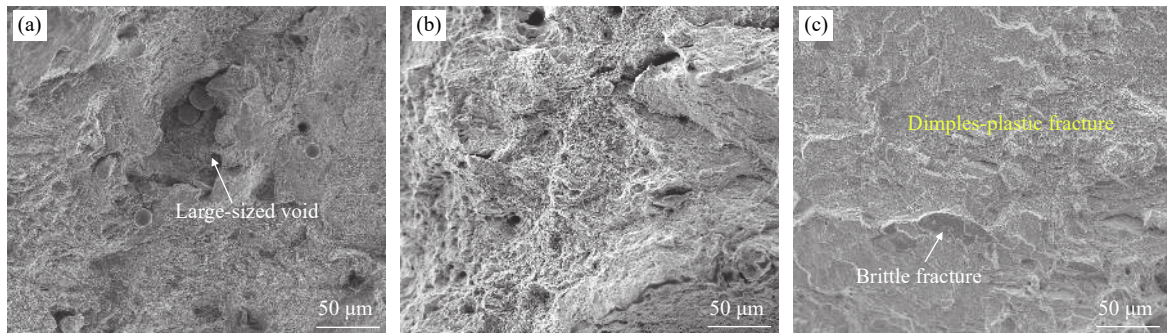
Fig. 12.   Characteristic fracture surfaces of compressive SMC samples produced using different laser scanning strategies: (a) CF; (b) NPF; (c) CBF.

or to that of SMC-CBF sample. This result indicated that the formation of cracks within the SMC-NPF sample was detrimental to their plastic deformability, because cracks resulting from large stresses were more irregularly shaped and angular than pores. The fracture surface of the SMC-NPF sample showed an uneven morphology characterized by dimples (Fig. 12(b)), which were deeper than those observed on the fracture surface of the SMC-CBF sample. Numerous small fracture zones initiated at defective sites with a high stress level and simultaneously connected with each other [38]. By contrast, the SMC-CBF sample showed a different fracture mechanism. The fracture surface of SMC-CBF showed a mixed fracture mode of dimple-plastic and brittle-fracture features (Fig. 12(c)). The CBF hatching mode entailed an increase in overlapping regions between separated small checkerboards and overlaps along the individual hatches. The overlapping regions between the checkerboards and individual hatches were generally considered as weak points for fracture due to the present defects and inherent tensile residual stresses [39]. Cracks most likely initiated from these weak points, which served as stress concentrators. The cracks subsequently propagated through the overlapping "network" [40]. The CBF hatching mode produced more overlapping regions within the SMC sample thus resulting in a lower compressive strength in SMC-CBF sample compared with the SMC-NPF sample.

Based on the above discussion, the CBF hatching mode is the most suitable to fabricate high-quality SMC samples. The main challenge to obtain fully dense CBF-SMC parts is to eliminate the formation of metallurgical defects between checkerboards. Setting an appropriate laser scan compensation value between checkerboards is a promising approach to overcome this challenge. A detailed investigation will be conducted in the near future to reveal the effect of laser compensation value on the processing quality and resulting mechanical properties of SMC-CBF sample.

5. Conclusions

(1) Laser scan strategies can greatly affect the processing quality of SLM-fabricated SMC components. When the SS sequence was employed, the MBE can be effectively alleviated, leading to an improved surface quality of the fabricated SMCs. By utilizing the IOS stagger mode, internal defects within SMCs were reduced, because the laser energy input at neighboring layers was distributed in a uniform manner. The OS stagger mode alleviated the stress accumulation along a single direction, preventing deviations from the intended component shape. When the SS laser scanning sequence was employed together with the IOS and OS stagger modes, highly dense SMC parts can be fabricated. However, undesired microcracks oriented perpendicular to the building direction formed within the SMC samples. When SMCs were fabricated using the CBF hatching mode, the evolution of residual stresses can be significantly reduced, preventing the formation of microcracks. Consequently, the SMC-CBF specimen showed a high densification level of 98.1%.

(2) Regardless of the employed laser scanning strategies, the microstructures of all SLM-fabricated SMCs were composed of martensite as the main phase and retained austenite with a low volume fraction. The content of retained austenite within SMCs depended on the hatching mode used. The SMC-CF sample contained retained austenite of about 27.8vol%, which was almost twice those of SMC-NPF (12.1vol%) and SMC-CBF (14.6vol%) samples. Different laser scanning strategies also caused varied thermal cycling behaviors during SLM, entailing different phase constitutions of SMC samples. The microstructure showed a cellular morphology with ring-like $(Fe,W)_6C$ carbides that formed along the cell boundaries. The laser scanning strategies significantly influenced the final morphologies of the Fe_2W_4C carbidic network. The carbidic network in NPF and CBF samples showed a decent continuity. The average sizes of the cell structures in NPF and CBF samples were 1.45 and 1.76 μm, respectively.

(3) Laser scan strategy significantly influenced the mechanical properties of the SLM-fabricated SMCs. The SMC-CF specimen exhibited the lowest compressive strength of ~2365.4 MPa and a limited fracture strain of ~21.2%. By contrast, the SMC-NPF sample demonstrated the highest

compressive strength of ~3184.3 MPa among all the tested samples and an improved fracture strain of ~23.5%. Nevertheless, the ductility of SMC-NFP sample was inferior to that of SMC-CBF sample (~24.8%). This finding indicated that the formation of cracks within the SMC-NFP sample was detrimental to the corresponding plastic deformability. Cracks are less regularly shaped and more angular than pores, and hence pose larger stress concentrators. The SMC sample fabricated using the CBF hatching mode showed the greatest potential to be pore- and crack-free. Setting an appropriate laser scan compensation value between checkerboards is a promising approach to further increase the density of SMC-CBF parts. A more detailed investigation about this strategy will be conducted in the near future.

Acknowledgements

References

[1] B. AlMangour, D. Grzesiak, and J.M. Yang, Scanning strategies for texture and anisotropy tailoring during selective laser melting of TiC/316L stainless steel nanocomposites, *J. Alloys Compd.*, 728(2017), p. 424.

[2] H.Y. Chen, D.D. Gu, H.M. Zhang, L.X. Xi, T.W. Lu, L. Deng, U. Kühn, and K. Kosiba, Novel WC-reinforced iron-based composites with excellent mechanical properties synthesized by laser additive manufacturing: Underlying role of reinforcement weight fraction, *J. Mater. Process. Technol.*, 289(2021), art. No. 116959.

[3] D.D. Gu, H.M. Zhang, D.H Dai, M.J. Xia, C. Hong, and R. Poprawe, Laser additive manufacturing of nano-TiC reinforced Ni-based nanocomposites with tailored microstructure and performance, *Composites Part B*, 163(2019), p. 585.

[4] X.Q. Ni, D.C. Kong, Y. Wen, L. Zhang, W.H. Wu, B.B. He, L. Lu, and D.X. Zhu, Anisotropy in mechanical properties and corrosion resistance of 316L stainless steel fabricated by selective laser melting, *Int. J. Miner. Metall. Mater.*, 26(2019), No. 3, p. 319.

[5] X.Q. Yang, Y. Liu, J.W. Ye, R.Q. Wang, T.C. Zhou, and B.Y. Mao, Enhanced mechanical properties and formability of 316L stainless steel materials 3D-printed using selective laser melting, *Int. J. Miner. Metall. Mater.*, 26(2019), No. 11, p. 1396.

[6] L. Fan, H.Y. Chen, Y.H. Dong, L.H. Dong, and Y.S. Yin, Wear and corrosion resistance of laser-cladded Fe-based composite coatings on AISI 4130 steel, *Int. J. Miner. Metall. Mater.*, 25(2018), No. 6, p. 716.

[7] F.Y. Niu, D.J. Wu, G.Y. Ma, and B. Zhang, Additive manufacturing of ceramic structures by laser engineered net shaping, *Chin. J. Mech. Eng.*, 28(2015), No. 6, p. 1117.

[8] B. AlMangour, D. Grzesiak, T. Borkar, and J.M. Yang, Densification behavior, microstructural evolution, and mechanical properties of TiC/316L stainless steel nanocomposites fabricated by selective laser melting, *Mater. Des.*, 138(2018), p. 119.

[9] B. AlMangour, D. Grzesiak, and J.M. Yang, Selective laser melting of TiC reinforced 316L stainless steel matrix nanocomposites: Influence of starting TiC particle size and volume content, *Mater. Des.*, 104(2016), p. 141.

[10] N. Kang, W.Y. Ma, L. Heraud, M.E. Mansori, F.H. Li, M. Liu, and H.L. Liao, Selective laser melting of tungsten carbide reinforced maraging steel composite, *Addit. Manuf.*, 22(2018), p. 104.

[11] X.C Yan, C.Y. Chen, R.X. Zhao, W.Y. Ma, R. Bolot, J. Wang, Z.M. Ren, H.L. Liao, and M. Liu, Selective laser melting of WC reinforced maraging steel 300: Microstructure characterization and tribological performance, *Surf. Coat. Technol.*, 371(2019), p. 355.

[12] J.D. Wang, L.Q. Li, and W. Tao, Crack initiation and propagation behavior of WC particles reinforced Fe-based metal matrix composite produced by laser melting deposition, *Opt. Laser Technol.*, 82(2016), p. 170.

[13] J.P. Kruth, L. Froyen, J.V. Vaerenbergh, P. Mercelis, M. Rombouts, and B. Lauwers, Selective laser melting of iron-based powder, *J. Mater. Process. Technol.*, 149(2004), No. 1-3, p. 616.

[14] W.X. Zhang, Y.S. Shi, B. Liu, L. Xu, and W. Jiang, Consecutive sub-sector scan mode with adjustable scan lengths for selective laser melting technology, *Int. J. Adv. Manuf. Technol.*, 41(2009), No. 7-8, art. No. 706.

[15] B. Qian, Y.S. Shi, Q.S. Wei, and H.B. Wang, The helix scan strategy applied to the selective laser melting, *Int. J. Adv. Manuf. Technol.*, 63(2012), No. 5-8, p. 631.

[16] X.B. Su and Y.Q. Yang, Research on track overlapping during selective laser melting of powders, *J. Mater. Process. Technol.*, 212(2012), No. 10, p. 2074.

[17] K.G. Prashanth, S. Scudino, and J. Eckert, Defining the tensile properties of Al–12Si parts produced by selective laser melting, *Acta Mater.*, 126(2017), p. 25.

[18] P. Mercelis and J.P. Kruth, Residual stresses in selective laser sintering and selective laser melting, *Rapid Prototyping J.*, 12(2006), No. 5, p. 254.

[19] S.A. Sillars, C.J. Sutcliffe, A.M. Philo, S.G.R. Brown, J. Sienz, and N.P. Lavery, The three-prong method: A novel assessment of residual stress in laser powder bed fusion, *Virtual Phys. Prototyping*, 13(2018), No. 1, p. 20.

[20] D. Buchbinder, W. Meiners, N. Pirch, K. Wissenbach, and J. Schrage, Investigation on reducing distortion by preheating during manufacture of aluminum components using selective laser melting, *J. Laser Appl.*, 26(2014), No. 1, art. No. 012004.

[21] Y. Liu, Y.Q. Yang, and D. Wang, A study on the residual stress during selective laser melting (SLM) of metallic powder, *Int. J.*

Adv. Manuf. Technol., 87(2016), No. 1-4, p. 647.

[22] D.H. Dai and D.D. Gu, Thermal behavior and densification mechanism during selective laser melting of copper matrix composites: Simulation and experiments, *Mater. Des.*, 55(2014), p. 482.

[23] X.C. Wang, T. Laoui, J. Bonse, J.P. Kruth, B. Lauwers, and L. Froyen, Direct selective laser sintering of hard metal powders: Experimental study and simulation, *Int. J. Adv. Manuf. Technol.*, 19(2002), No. 5, p. 351.

[24] M. Badrossamay and T.H.C. Childs, Further studies in selective laser melting of stainless and tool steel powders, *Int. J. Mach. Tools Manuf.*, 47(2007), No. 5, p. 779.

[25] Y.H. Xiong, W.H. Hofmeister, Z. Cheng, J.E. Smugeresky, E.J. Lavernia, and J.M. Schoenung, *In situ* thermal imaging and three-dimensional finite element modeling of tungsten carbide–cobalt during laser deposition, *Acta Mater.*, 57(2009), No. 18, p. 5419.

[26] B.J. Keene, Review of data for the surface tension of pure metals, *Int. Mater. Rev.*, 38(1993), No. 4, p. 157.

[27] A. Hussein, L. Hao, C.Z. Yan, and R. Everson, Finite element simulation of the temperature and stress fields in single layers built without-support in selective laser melting, *Mater. Des.*, 52(2013), p. 638.

[28] D.D. Gu and Y.F. Shen, Balling phenomena during direct laser sintering of multi-component Cu-based metal powder, *J. Alloys Compd.*, 432(2007), No. 1-2, p. 163.

[29] B. Cheng, S. Shrestha, and K. Chou, Stress and deformation evaluations of scanning strategy effect in selective laser melting, *Addit. Manuf.*, 12(2016), p. 240.

[30] D. Wang, C.H. Song, Y.Q. Yang, and Y.C. Bai, Investigation of crystal growth mechanism during selective laser melting and mechanical property characterization of 316L stainless steel parts, *Mater. Des.*, 100(2016), p. 291.

[31] M. Shiomi, K. Osakada, K. Nakamura, T. Yamashita, and F. Abe, Residual stress within metallic model made by selective laser melting process, *CIRP Ann.*, 53(2004), No. 1, p. 195.

[32] N.K. Tolochko, M.K. Arshinov, A.V. Gusarov, V.I. Titov, T. Laoui, and L. Froyen, Mechanisms of selective laser sintering and heat transfer in Ti powder, *Rapid Prototyping J.*, 9(2003), No. 5, p. 314.

[33] M.L. Zhong, H.Q. Sun, W.J. Liu, X.F. Zhu, and J.J. He, Boundary liquation and interface cracking characterization in laser deposition of Inconel 738 on directionally solidified Ni-based superalloy, *Scripta Mater.*, 53(2005), No. 2, p. 159.

[34] H.Y. Chen, D.D. Gu, D.H. Dai, M.J. Xia, and C.L. Ma, A novel approach to direct preparation of complete lath martensite microstructure in tool steel by selective laser melting, *Mater. Lett.*, 227(2018), p. 128.

[35] H.Y. Chen, D.D. Gu, L. Deng, T.W. Lu, U. Kühn, and K. Kosiba, Laser additive manufactured high-performance Fe-based composites with unique strengthening structure, *J. Mater. Sci. Technol.*, (2020). DOI: 10.1016/j.jmst.2020.04.011

[36] Y.M. Wang, T. Voisin, J.T. McKeown, J.C. Ye, N.P. Calta, Z. Li, Z. Zeng, Y. Zhang, W. Chen, T.T. Roehling, R.T. Ott, M.K. Santala, P.J. Depond, M.J. Matthews, A.V. Hamza, and T. Zhu, Additively manufactured hierarchical stainless steels with high strength and ductility, *Nat. Mater.*, 17(2018), No. 1, p. 63.

[37] J.W. Cahn, The impurity-drag effect in grain boundary motion, *Acta Metall.*, 10(1962), No. 9, p. 789.

[38] A. Inoue, B.L. Shen, and C.T. Chang, Super-high strength of over 4000 MPa for Fe-based bulk glassy alloys in $[(Fe_{1-x}Co_x)_{0.75}B_{0.2}Si_{0.05}]_{96}Nb_4$ system, *Acta Mater.*, 52(2004), No. 14, p. 4093.

[39] T. Niendorf, S. Leuders, A. Riemer, H.A. Richard, T. Tröster, and D. Schwarze, Highly anisotropic steel processed by selective laser melting, *Metall. Mater. Trans. B*, 44(2013), No. 4, p. 794.

[40] J. Suryawanshi, K.G. Prashanth, S. Scudino, J. Eckert, O. Prakash, and U. Ramamurty, Simultaneous enhancements of strength and toughness in an Al–12Si alloy synthesized using selective laser melting, *Acta Mater.*, 115(2016), p. 285.